Realizing Generalized Brewster Effect by Generalized Kerker Effect

Zhe Zhang,[1] Zhiyuan Che,[1] Xiuye Liang,[1] Jiao Chu,[1] Jianping Zeng,[2] Hao Huang,[2] Fang Guan,[2,3,*]
Lei Shi,[1,4,†] Xiaohan Liu,[1] and Jian Zi[1,4]

[1] *State Key Laboratory of Surface Physics, Key Laboratory of Micro- and Nano-Photonic Structures (Ministry of Education) and Department of Physics, Fudan University, Shanghai 200438, China*
[2] *Institute for Nanoelectronic Devices and Quantum Computing and Zhangjiang Fudan International Innovation Center, Fudan University, Shanghai 200438, China*
[3] *Peng Cheng Laboratory, Shengzhen 518000, China*
[4] *Collaborative Innovation Center of Advanced Microstructures, Nanjing University, Nanjing 210093, China*

(Received 23 July 2021; revised 16 September 2021; accepted 8 October 2021; published 8 November 2021)

A simple and universal design principle to realize the generalized Brewster effect (GBE) is proposed. Based on the generalized Kerker effect (GKE), we can realize the GBE for arbitrary polarizations, any incident angles, and any frequencies on the traditional dielectric interface by the destructive interference of various of multipoles. An adjustable metallic meta-surface has been designed to achieve this effect experimentally in the microwave band. By adjusting the suspension height of meta-surfaces above the interface, the incident angles and frequency corresponding to the GBE can be modulated easily. For the two different polarized incident waves, the GBE can be realized at the same frequency and same incident angle, which shows the validity of the GKE. This design principle opens the door for realizing tunable GBE devices that can be applied in many scenarios.

DOI: 10.1103/PhysRevApplied.16.054017

I. INTRODUCTION

In the 1810s, Brewster [1] found a phenomenon that p-polarized light (that is, the electric field vector parallel to incident plane) will vanish in reflected light when unpolarized light impinges onto a homogenous isotropic nonmagnetic dielectric interface with a specific incident angle which is known as Brewster's angle (BA) θ_B. In fact, based on the Fresnel principle, s-polarized light (that is, the electric field vector is perpendicular to the incident plane) can also vanish in reflected light when it impinges onto a magnetic material ($\mu_r \neq 1$) interface [2]. However, the magnetic materials are all in the microwave band and have strong absorption. To realize tunable magnetic responses with low absorption, metamaterials have been proposed [3–12]. The most amazing thing is that people can subtly design meta-atoms that have multiple degrees of freedom to adjust relative permittivity ε_r or relative permeability μ_r of metamaterials. According to complex electromagnetic responses of metamaterials, researchers have proved the existence of the Brewster effect of s-polarized electromagnetic waves in many different systems [13–17]. In addition, researchers have also designed anisotropic and bianisotropic metamaterials that realize the Brewster effect for both s and p polarization [18,19]. Researchers called this phenomenon which s and p polarization with no reflection on the interfaces at specific angles as the generalized Brewster effect (GBE) [20–24], and the specific incident angle is known as the generalized Brewster angle (GBA).

Recently, as a kind of ultrathin metamaterial, meta-surfaces have attracted increased attention owing to their broad application prospects [11,25–32]. The GBE has also been realized in meta-surface systems [33–36]. In Ref. [22], based on the classical Kerker effect (CKE), the authors proved the GBE of a Si sphere meta-surface theoretically and experimentally. This brought attention to the GBE designed by the CKE which have a broader range of applications, such as cavity mirrors, amplitude and phase modulators [23,37], Brewster angle microscopes [38], and surface physics [39]. As is well known, the CKE only includes the interference of the electric dipole and magnetic dipole [40]. Definitely, almost all previous works have shown that both electric and magnetic multipolar responses in the metamaterials or meta-surfaces themselves are really indispensable for realizing the GBE. How the GBE can be realized at the same frequency and same incident angle for the two different polarized incident waves has hardly ever been studied. Recently, researchers have proposed that the generalized Kerker effect includes

---

[*] fguan@fudan.edu.cn
[†] lshi@fudan.edu.cn

omnidirectional interference of all low or high multipolar components which are not limited to electromagnetic couplings [41]. This leads us to ask: to realize the GBE, are both electric and magnetic multipolar responses in the structures really essential? Can the structures which have either electric or magnetic responses realize the dual-polarized GBE for the same frequency and incident angle simply by the GKE?

In this paper, based on the GKE, we propose a universal design method that is not just restricted by both electric and magnetic multipolar responses in structures to realize an arbitrary tunable GBE. First, we show that the reflection on the interface can be equivalent to the radiation of an infinite-dipole phased array. Then, for realizing an s-polarized GBE, we add an artificial adjustable either electric or magnetic dipole array to realize a destructive interference with the equivalent dipole array on the interface at any inspired direction. For realizing a p-polarized GBE, we can also use a similar electric or magnetic dipole array to cancel the reflected wave at any inspired direction, or we can use intrinsic classical Brewster effect (CBE) which is determined by the difference of relative permittivity for the two kinds of medium. For the simultaneous realization of an s- and p-polarized GBE, we can combine the above modulated methods of two polarizations through a two-layer array with orthogonal resonances, that is, the radiation from the artificial dipole array we add can just interfere with the single-polarized reflected wave. In principle, by analyzing and adjusting the total far-field radiated situations in one unit cell, the condition of the GKE which is unrelated to incident polarizations can be satisfied in any desired direction and frequency by adjusting the suspension height above the interface of the dipole array we add. We have designed several kinds of metallic meta-surfaces to demonstrate our theory in the microwave band. We have fabricated the designed structures on top of a dielectric trapezoidal prism with a pyramid-array antireflection slab, and measured the reflected property through a microwave tested system. The structures are compact and have a low profile. The experimental results, which agree well with the simulation, show that: for s polarization, we can realize the GBE in almost all incident angles ($\theta = 10^{\circ} \sim 85^{\circ}$) and incident planes ($\varphi = 0^{\circ}$–$90^{\circ}$) by adjusting the suspension height from 1.1 to 4.7 mm (lower than half of the center wavelength); for s- and p-polarization, we can realize the GBE at incident angles $\theta = 20^{\circ}$–60° by adjusting suspension height from 1.2 to 6.5 mm (smaller than half of the center wavelength basically). It is noted that the incident angle and frequency of realization of the GBE can be modulated easily at any time, rather than adjusting the geometric parameters and so on which may force designers to refabricate samples. It is shown that our design method really has potential for the realization of easy-to-integrate tunable GBE devices.

II. DESIGN PRINCIPLE AND METHOD BASED ON THE GENERALIZED KERKER EFFECT

As shown in Figs. 1(a) and 1(d), an s- or p-polarized plane wave impinges onto medium 2 ($\varepsilon_r \neq 1, \mu_r = 1$) from medium 1 (in this work it is air, $\varepsilon_r = 1, \mu_r = 1$) at an angle. The traditional interpretation of the BA is that an incident plane electromagnetic wave can excite equivalent electric dipoles whose vibrated direction is the same as the incident electric field direction on the interface. For a p-polarized plane wave, when the vibrated direction of these equivalent electric dipoles (as shown in Fig. 1(d), red double-sided arrows) in the incident plane are the same as the reflected direction, there is no reflection because of zero radiation of the electric dipole array in this direction, which is called the CBE. However, for an s-polarized plane wave, because the vibrated direction of equivalent electric dipoles (as shown in Fig. 1(a), red cross-circle) is always perpendicular to the incident plane, the radiation is never zero in any direction, which is a result of no CBE being generated. In fact, based on Huygens' principle and infinite plane phased array theory, we can equate reflection and refraction of the plane wave with the radiation of an infinite discrete electric dipole phased array which is located on the interface [22,42,43] (the details are presented in Appendix A). It is worth noting that the refraction in dielectric can also be described through the radiation of an infinite dipolar phased array [44]. However, the related radiated patterns are not shown, because this work only discusses the situations in space above the interface.

The aforementioned contents inspired the idea that perhaps we can add artificial structures which can be equivalent to multipolar components to have a destructive interference with the equivalent dipoles on the interface. In general, the basic models which are shown in Fig. 1 can be summarized by two different situations. The first situation, shown in Figs. 1(b) and 1(c), is the s-polarized GBE. The other situation, shown in Figs. 1(e) and 1(f), is the p-polarized GBE. Apparently, the s- and p-polarized GBEs can both be realized by adding artificial structures. Thus, this indicates that the dual-polarized GBE can be realized by combining the two different situations. The previous works often combined the setups shown in Figs. 1(c) and 1(e) to realize a dual-polarized GBE. These artificial structures themselves have simultaneous electric and magnetic dipole responses no matter what the incident polarization is. The interference of electric and magnetic dipoles has been called the CKE. In general, based on the GKE, our methods are that we can combine more situations, such as those shown in Figs. 1(b) and 1(d), Figs. 1(c) and 1(f), and so on, which include all potential possibilities. It is noted that the example of a p-polarized CBE as shown in Fig. 1(d) can also be combined with another s-polarized situation to realize the dual-polarized GBE. The suspension height of structures above the interface

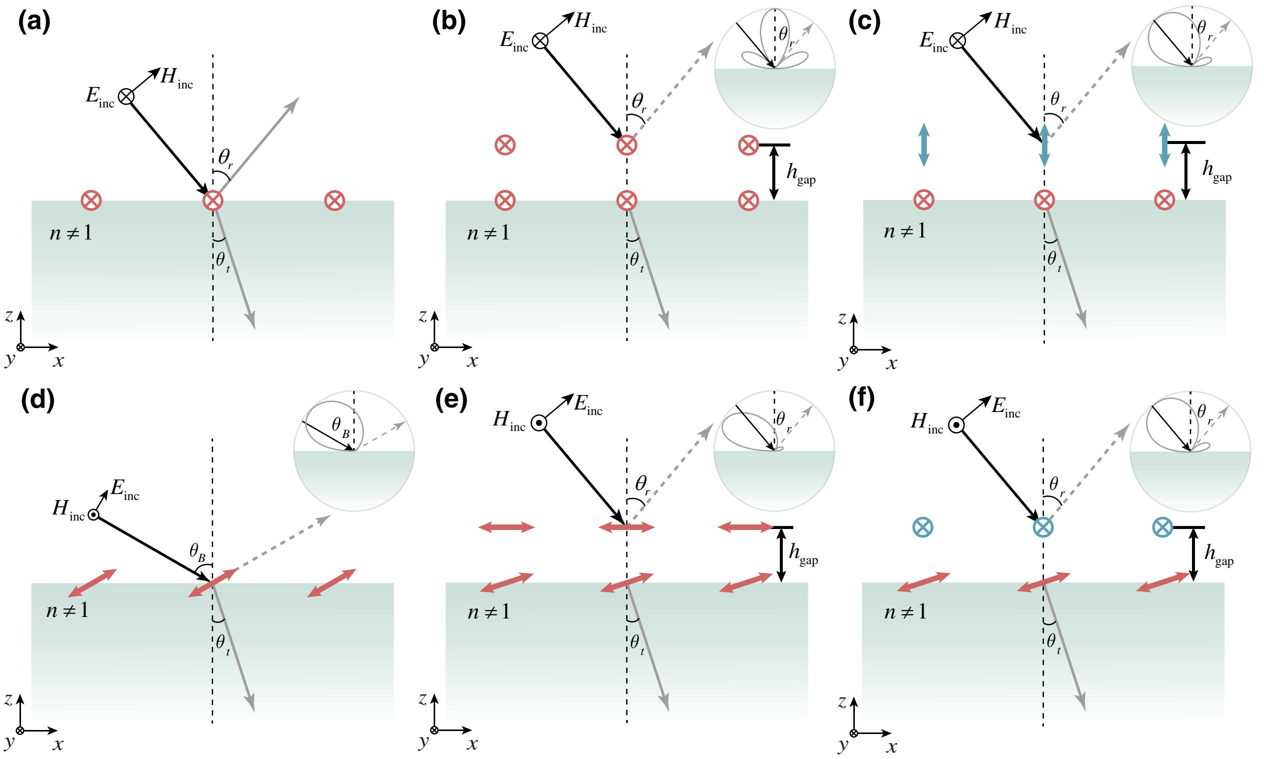

FIG. 1. The equivalent dipole models and interference models which can realize the GBE of arbitrary polarization based on the GKE. The red cross-circles and double-sided arrows represent equivalent electric dipoles, and the blue symbols represent equivalent magnetic dipoles. Dipoles suspended above the interface height $h_{\rm gap}$ come from the structures we add, and dipoles on the interface come from equivalence of the reflection and refraction waves. (a) The s-polarized plane wave impinges onto medium 2 at an angle. The representations of equivalent electric dipoles which vibrate in the same direction as incident electric fields. (d) There is no reflection when a p-polarized plane wave impinges onto medium 2 at angle θ_B. (b),(c) The incidence of the s-polarized electromagnetic wave and (e),(f) the incidence of the p-polarized electromagnetic wave. The patterns in the five insets which all have a zero point in the reflection direction represent the total radiation patterns of dipoles in one unit cell, respectively.

can be adjusted to modulate the GBE. To realize the dual-polarized GBE at the same angle and same frequency, the most important premise is that the electric and magnetic responses of the structures we add are independent and adjustable, respectively, for different polarizations.

Next, we give a specific analysis to illustrate our methods based on the GKE as an example. Thanks to the radiation pattern multiplication principle of an infinite phased array [22,45,46], an important and convenient way we can use is that zero in the reflection direction of the total radiation far-field of all multipolar components in each unit cell can give rise to zero radiation of the entire phased array in this direction. In other words, we can design the relative magnitude and phase of all multipolar components in one unit cell to realize GBE conveniently.

A simple generalized total electric far-field in one unit cell can be expressed [44] as

$$\boldsymbol{E}^{\rm total} = \boldsymbol{E}^{\rm equ} + \sum_{i=1}^{n} \boldsymbol{E}^{\rm add} \tag{1}$$

where $\boldsymbol{E}^{\rm total}$ is the total radiated electric far field in one unit cell, $\boldsymbol{E}^{\rm equ}$ is the radiated electric far-field of the equivalent dipole on the interface, and $\sum_{i=1}^{n} \boldsymbol{E}^{\rm add}$ is the total radiated electric far-field of the structures we add.

Now we choose the situation in Fig. 1(c) to obtain the expressions when the GBE is realized by Eq. (1). The total electric radiated far-field in the reflection direction can be obtained from the sum of Eqs. (C1) and (C2):

$$\begin{aligned} E_{\varphi}^{\rm total} &= E_{p1\varphi}^{\rm equ} + E_{m\varphi}^{\rm add} \\ &= \frac{k_0^2 e^{ik_0 r}}{4\pi\varepsilon_0 r}[(1+r_s)\,p_{y1}^{\rm equ} + \sqrt{\mu_0\varepsilon_0}e^{-ik_0 h_{\rm gap}\cos\theta_i} \\ &\quad \times \left(1 + r_s e^{ik_0 2h_{\rm gap}\cos\theta_i}\right) m_z^{\rm add}\sin\theta_i], \end{aligned} \tag{2}$$

where θ_i is the incident angle. According to the condition of the GKE, that is, $E_{\varphi}^{\rm total}|_{\theta=\theta_i} = 0$, we can obtain

$$\frac{m_z^{\rm add}}{p_{y1}^{\rm equ}} = -\frac{(1+r_s)\,e^{ik_0 h_{\rm gap}\cos\theta_i}}{\sqrt{\mu_0\varepsilon_0}\left(1 + r_s e^{ik_0 2h_{\rm gap}\cos\theta_i}\right)\sin\theta_i}. \tag{3}$$

In Eq. (3), $m_z^{\text{add}}/p_{y1}^{\text{equ}}$ can be a function of h_{gap}, θ_i, and frequency. In words, for the GBE which we want to realize at one incident angle θ_i, we can adjust h_{gap} to satisfy Eq. (3) (the specific discussions are presented in Appendix B) as shown in Fig. 1(c). The insets in Figs. 1(b), 1(d), and 1(f) can also validate our methods (the details of other examples are shown in Appendix C). In general, it is worth noting that the artificial dipole components which are shown in Figs. 1(b)–1(f) can be replaced to satisfy the condition of the GKE by other more multipolar components, such as dipoles with different vibrated directions, higher-order multipolar components, and so on.

III. META-SURFACE STRUCTURES AND NUMERICAL RESULTS

In this section, using the combinations of Figs. 1(c) and 1(d), and Figs. 1(c) and 1(f), we have designed meta-surface structures to realize the GBE. To validate the principle we have proposed, we demonstrate the modulated ability of suspension height of structures for different incident angles and polarizations.

A. Individual modulations of an s-polarized incident electromagnetic wave

As shown in Fig. 2(a), the shape of the metallic structure we designed resembles a letter “S.” The whole array is arranged in a square lattice of period p suspended in air above the interface height h_{gap} as shown in Fig. 2(b). All relevant parameters are listed in Table I. To reduce the influence of absorption from materials, simulations and experiments for all structures in this work are achieved in the millimeter wave band. In the state of absence of structures, when the p-polarized plane wave impinges onto the dielectric interface ($\varepsilon_{r1} = 3.5$, $\mu_r = 1$) from air, the BA is $\theta_B \approx 62^\circ$. After adding this structure, as shown in Fig. 2(c), when the s-polarized plane wave impinges at an angle $\theta = 62^\circ$, the GBE will be realized at different frequencies for all incident planes ($\varphi = 0^\circ \sim 90^\circ$). As shown in Fig. 2(d), when the p-polarized plane wave impinges at the same incident angle $\theta = 62^\circ$, it is pretty obvious that reflectance at any frequencies for all incident planes is very close to zero. Next, as shown in Fig. 2(e), for three frequencies ($f_{\varphi=0^\circ} = 28.5$ GHz, $f_{\varphi=45^\circ} = 28.9$ GHz, $f_{\varphi=90^\circ} = 29.25$ GHz), s- and p-polarized GBAs are nearly equal in three incident planes ($\varphi = 0^\circ, 45^\circ, 90^\circ$, respectively).

To analyze the multipolar components excited by the incident wave when the GBE was realized, first we extract the volume electric current density of the S ring in one unit cell at $\varphi = 0^\circ$, $\theta = 62^\circ$, $f = 28.5$ GHz [brown circle in Fig. 2(e)]. The first part of Fig. 2(f) shows that when the s-polarized plane wave impinges, based on the right-hand rule, the electric current density of the S ring rotates in the same direction (see the lilac arrows in this figure) around centers of the two half-rings, respectively, resulting in a superposed induced magnetic field of the two half-rings that can be equivalent to a strong magnetic dipole. However, the strength of electric dipoles is very weak because of the reverse direction of the electric current density. Thus, the total multipolar component of this structure in the s-polarized situation is an almost magnetic dipole along the z axis direction. The second part of Fig. 2(f) shows that, when the p-polarized plane wave impinges, the electric current density of the S ring rotates in the reverse direction (lilac arrows) around centers of the two half-rings, respectively, resulting in a counteracted induced magnetic field of the two half-rings that can be equivalent to a weak magnetic dipole. Owing to the weak electric current density, the electric dipole components are also weak. In the p-polarized situation, every multipole components of this structure are very weak, corresponding to the structure hardly responding for the incidence of the p-polarized wave. This explains that the GBE can be realized at any frequency for all incident planes when the incident angle is $\theta = 62^\circ$ as shown in Fig. 2(d). In Fig. 2(g), the radiation pattern of each equivalent multipole component in one unit cell was analyzed on the basis of the volume electric current density of the S ring as shown in the first schematic of Fig. 2(f) [12,47–49]. Apparently, there is a zero point along the reflected direction (dashed line arrow, $\theta = 62^\circ$).

In fact, the adjustments of h_{gap} definitely modulate multipolar components of structures above the interface [50]. As theoretical proofs in Sec. II and Appendix B, we show that the magnitude and phase of the multipolar components which are needed to realize the GBE are quite relevant to h_{gap}. The s-polarized GBA can be modulated when adjusting suspension height h_{gap} of the structure. For example, the four curves correspond to different GBAs which are $\theta_{\text{GB}} = 10^\circ, 35^\circ, 60^\circ$, and 85°, respectively, as shown in Fig. 3(a). It can be seen that the adjustable range of the GBA is very wide. Figure 3(b) shows that there is definitely a zero point in the total far-field pattern along the reflected direction for different suspension height h_{gap} corresponding to the reflection direction, respectively, resulting in the realization of the s-polarized GBE for the whole system.

The arrangement of the S ring meta-surface shown in Figs. 2(a) and 2(b) only has 180° rotation symmetry, resulting in electromagnetic responses of the structure being different for changeable incident planes, as shown in Fig. 2(c). It is conceivable that if symmetry of the whole array can be increased, the problem of different responses for different incident planes may be solved. These arrangements, which are shown in Figs. 4(a) and 4(b), have identical parameters to those listed in Table I. As shown in Figs. 4(c) and 4(d), the GBE was realized in all incident planes ($\varphi = 0^\circ$–90°) at almost the same frequency ($f = 28.85$ GHz) when the s-polarized plane wave impinges at angle $\theta = 62^\circ$. Similar to Fig. 2(d), the responses are really very weak for incidence of a p-polarized wave at the same

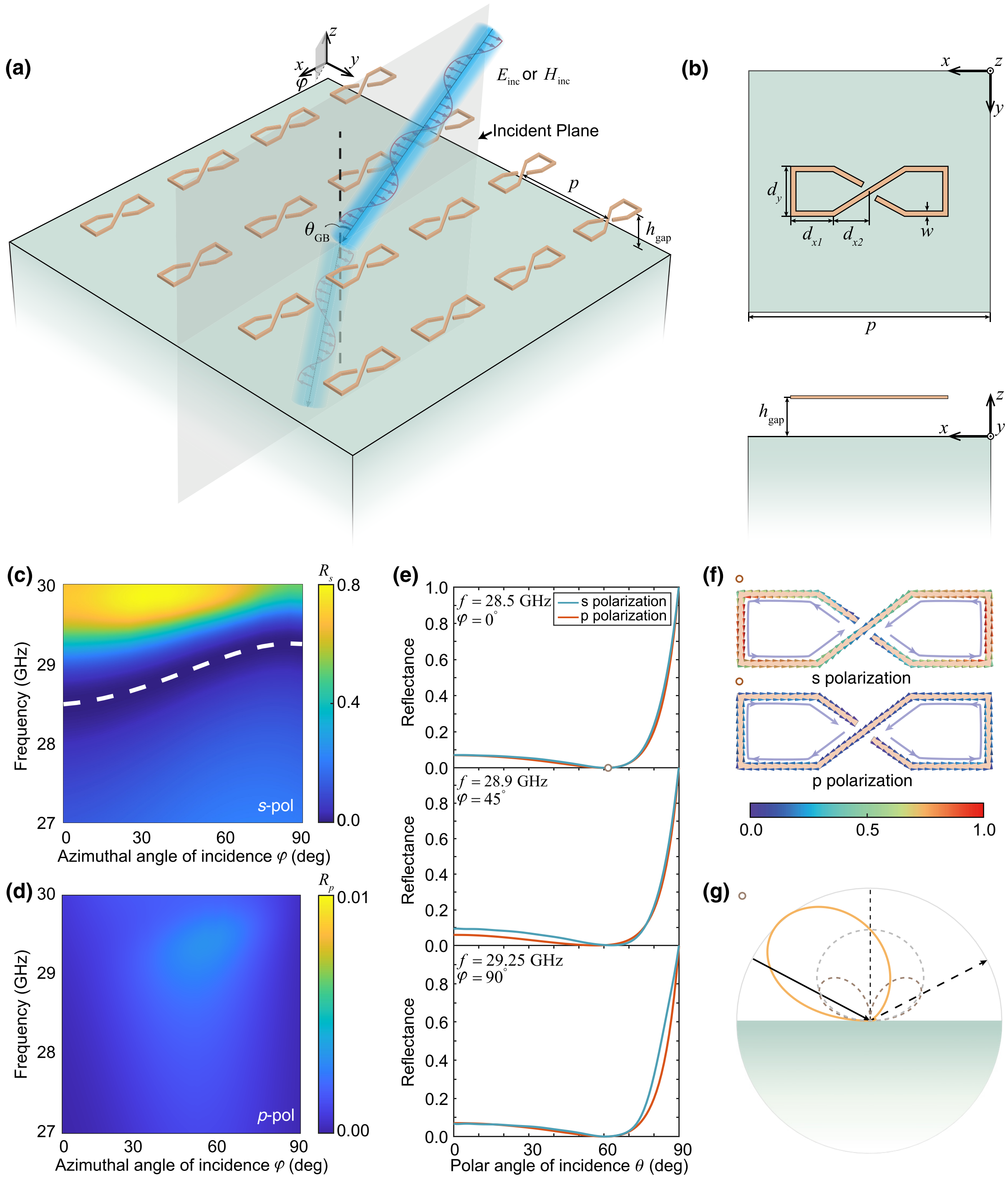

FIG. 2. Schematic and simulated results of an S ring meta-surface. (a),(b) S ring meta-surface suspends above the interface height h_{gap}. The relative permittivity and permeability of dielectric which is full of lower half-space are $\varepsilon_{r1} = 3.5$, $\mu_{r1} = 1$, respectively. (c) The reflectance R_s as a function of azimuthal angle of incidence φ and frequency when an s-polarized plane wave impinges at angle $\theta_i = 62^\circ$. The white dashed line indicates the GBA of s polarization from $\varphi = 0^\circ$ to $\varphi = 90^\circ$. (d) The reflectance R_p as a function of azimuthal angle of incidence φ and frequency when a p-polarized plane wave impinges at incident angle $\theta_i = 62^\circ$. (e) At the frequency of realization of the GBE corresponding to the white dashed line as shown in Fig. 2(c), the reflectance of s and p polarization as a function of incident angle, respectively, when incident planes are $\varphi = 0^\circ, 45^\circ, 90^\circ$, respectively. (f) At $\varphi = 0^\circ, \theta = 62^\circ, f = 28.5$ GHz [brown circle in Fig. 2(e)], the electric current density distributions of an S ring when a dual-polarized GBE is realized. (g) The radiation pattern A (brown) of a multipole expansion of the volume electric current density in the first schematic excited by s polarization as shown in Fig. 2(e). The radiation pattern B (gray) of the electric dipole equivalent to the reflection plane wave. The total radiation pattern C (yellow) obtained by the sum of patterns A and B.

TABLE I. The geometric parameters of the structure as shown in Figs. 2(a) and 2(b).

Parameters	d_{x1}	d_{x2}	d_y	h_{gap}	p	w
Value/mm	1.1	0.67	1	1.88	5	0.1

incident angle, with the result that the GBE can be realized at the whole frequency range. As shown in Fig. 4(e), for the s-polarized GBE at $f = 28.85$ GHz, the reflectance of dual-polarized waves as functions of the incident angle θ are almost identical for three different incident planes, $\varphi = 0^\circ$, 45°, and 90°. It is apparent that all GBAs which are marked by a black dashed line are $\theta = 62^\circ$ for the three different situations. The details about the high-order diffractions of this structure in Figs. 2(a) and 2(b) are presented in Appendix E.

B. Arbitrary modulation of a both s- and p-polarized electromagnetic wave

In order to realize the dual-polarized GBE, from the combination of Figs. 1(c) and 1(f), we designed another two-layer S ring meta-surface. From the previous analysis, this structure can be equivalent to a magnetic dipole along the z axis direction for s-polarized incident wave, but it is hardly excited by a p-polarized wave. Taking the incident plane $\varphi = 0^\circ$ as an example, the direction of the magnetic field of the p-polarized incident wave is perpendicular to the x–z plane. If the surface of the S ring is parallel to the x–z plane, it can be excited by the incidence of a p-polarized plane wave in theory.

The S rings are arranged as shown in Fig. 5(a) with period of $p = 5$ mm. The suspension height h_{gap} and h_{gap2} of the dual-layer structures can be adjusted to modulate the GBE flexibly. The simulated results of reflectance versus incident angle are shown in Fig. 5(c) which correspond to changeable GBA ($\theta_{\text{GB}} = 20^\circ, 35^\circ, 50^\circ$) by freely controlling the h_{gap} and h_{gap2} for s- and p-polarized incident waves. As shown in the two left schematics of Fig. 5(b), when the s-polarized plane wave impinges, the electric current density of rings A and B rotate in the same direction (the lilac arrows as shown in the second schematic) around centers of the two half-rings, respectively. However, the electric current density of ring A is very weak. Based on the right-hand rule, the magnetic dipole component of ring A is far weaker than the ring B. Thus, apparently, in this situation multipolar components of the whole of structures almost magnetic dipoles along the z direction. As shown in the two right schematics of Fig. 5(b), when the p-polarized plane wave impinges, the strength of current density of ring A is far bigger than ring B, resulting in the multipolar components of the whole structure in this situation being almost magnetic dipoles along the y axis direction. As shown in Fig. 5(d), apparently, the zero points along the reflected direction in the total far-field pattern for realizing a both s- and p-polarized GBE simultaneously. The results in this section can effectively validate the equivalent theoretical models as stated in Sec. II.

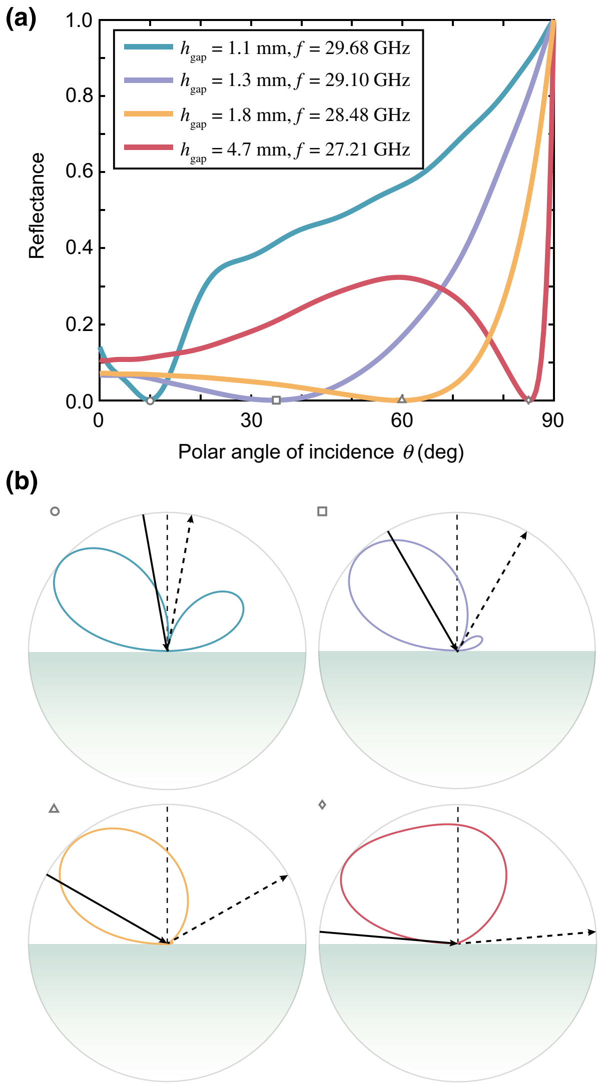

FIG. 3. Variations of the s-polarized GBA through the adjustments of h_{gap} in the incident plane $\varphi = 0^\circ$ for the structure as shown in Fig. 2(a). (a) Reflectance as a function of angle of incidence θ corresponding to $h_{\text{gap}} = 1.1, 1.3, 1.8, 4.7$ mm. GBAs are $\theta_{\text{GB}} = 10^\circ, 35^\circ, 60^\circ, 85^\circ$ at relevant frequencies, respectively. (b) For the four different situations in which the GBE was realized as shown in Fig. 3(a), the total radiation patterns respectively come from the sum of radiated far-field of multipole expansion of the structure's volume density and equivalent electric dipole of the reflection wave.

IV. EXPERIMENTAL VERIFICATIONS

As shown in Fig. 6(a), the experimental instruments are designed to perform detection of reflectance in the millimeter band. Two standard gain horn antennas which are

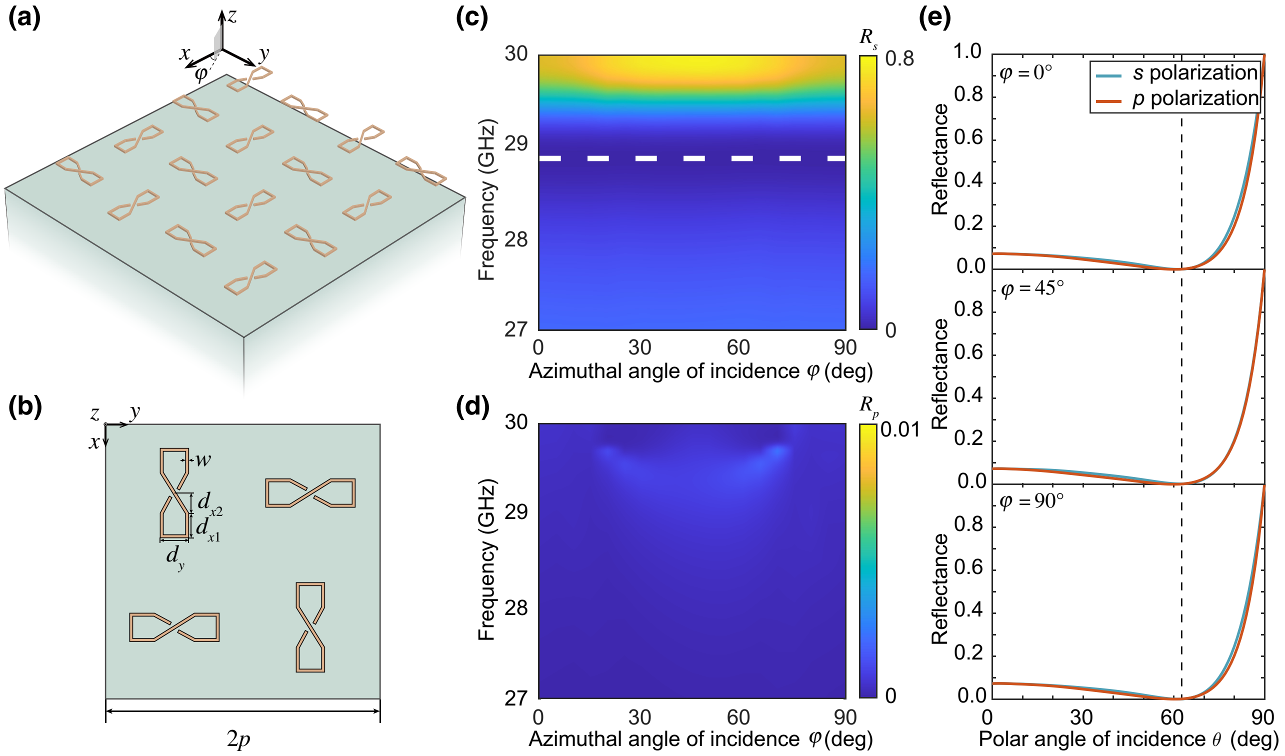

FIG. 4. Schematic and simulated results of 90° symmetrical S ring meta-surface. (a),(b) The S ring structures whose parameters are listed in Table I are arranged with 90° rotational symmetry periodically. (c),(d) The reflectance as a function of azimuthal angle of incidence φ and frequency when the s- or p-polarized plane wave impinges at angle $\theta = 62^\circ$. The white dashed line indicates the GBA of s polarization from $\varphi = 0^\circ$ to $\varphi = 90^\circ$. (e) At $f = 28.85$ GHz, the reflectance of two polarization waves as functions of the incident angle θ when incident planes are $\varphi = 0^\circ, 45^\circ, 90^\circ$, respectively.

connected to the two ports of a vector network analyzer (VNA, N5245B) are fixed on the removable supports that are symmetrical about the normal of diameter along the semicircle slideway. The samples are fixed on the top of the trapezoidal prism which are both placed at center of the semicircle to assure the incident angle θ_i is equal to the reflected angle θ_r. To change the suspension height of samples and support the samples, polymethacrylimide (PMI) foam slabs ($\varepsilon_r \approx 1$) are used. By rotating the two horns 2.5° at a time, an s_{12} spectrum is measured by the VNA. The biggest range of incident angle is $\theta_i = 5^\circ$–80°. Through rotating the apertures of two horns, the transformations of s and p polarization can be realized separately. As the proposed methods and results are studied on the interface of two semi-infinite media, it is indeed difficult to make a similar substrate relative to the wavelength in the millimeter wave band. Thus, some equivalent methods are designed for the entire test to furthest minimize the influence of finite thickness substrates for experimental results (the design methods of special substrate are shown in Appendix D).

As shown in Figs. 6(b) and 6(c), four kinds of samples were fabricated in this work. For the purpose of fabricating and testing conveniently, as well as reducing the effect of substrates extremely, in this work all metallic structures were printed on the thinnest substrates (Rogers RT / duroid 5880) which have the lowest permittivity through printed circuit board (PCB) technology. As shown in Fig. 6(b), ①②③ are three kinds of planar samples (60 × 60 array) with the same geometric parameters and different arrangements of unit cells. Sample ①; corresponds to Fig. 2(a). Samples ② and ③ both correspond to Fig. 4(a), which presented different incident planes ($\varphi = 0^\circ, 45^\circ$, respectively). The planar samples are fixed on the top of PMI foam slabs, with thickness represented by h_{gap}. The geometric parameters are specifically listed in Table II. As shown in Fig. 6(c), this dual-layer structure is composed of samples ① and ④. This dual-layer structure corresponds to Fig. 5(a). Sample ④ is composed of 60 PCB belts whose surfaces were printed S rings with the same geometric parameters as listed in Table II except for $d_y = 1.25$ mm. For each PCB belt, the thickness is $h = 0.254$ mm and width is $w_{\text{belt}} = 2$ mm. Each PCB belt was tightly fixed on the side of a narrow PMI foam strip of thickness $h_{\text{PMI strip}} = 4.45$ mm. In addition, all strips and PCB belts are also fixed on the top of a PMI slab of thickness $h_{\text{PMI slab}} = 2$ mm. The suspension height of sample ④ is represented by h_{gap2}.

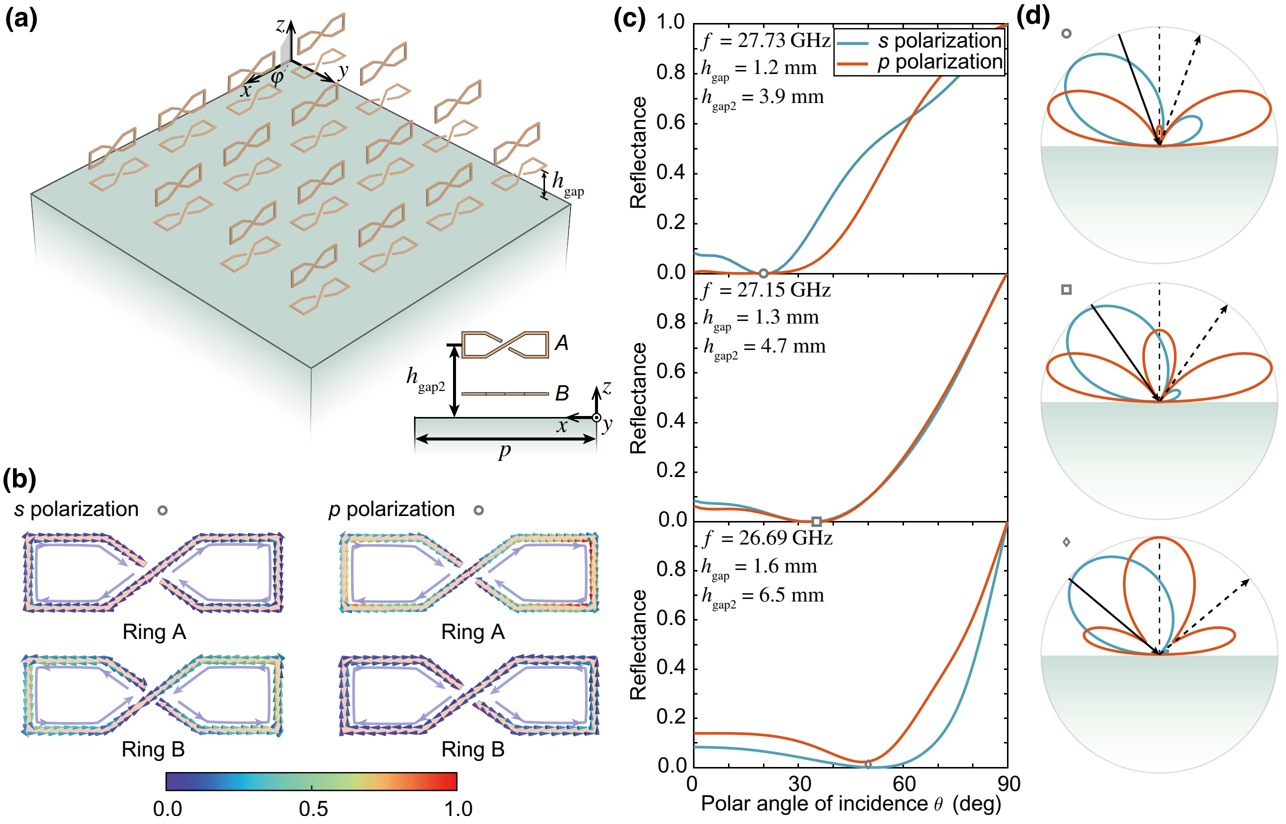

FIG. 5. Schematic and simulated results of the dual-layer S ring meta-surface. (a) The S ring structures are arranged in two layers periodically. The arrangement of bottom-layer structures is the same as Fig. 2(a), but the top-layer structures are arranged perpendicular to the interface. The inset shows a side view of the relative position of two rings in one unit. The suspension height of rings A and B are h_{gap2} and h_{gap}, respectively. (b) The volume electric current density of rings A and B when the two polarization plane waves impinge at an angle $\theta = 20^\circ$ corresponding to the situation of Fig. 5(c). The two figures on the left show electric current density for an s-polarized wave. The two figures on the right show electric current density for a p-polarized wave. (c) The reflectance as a function of the incident angle when the GBAs are $\theta = 20^\circ, 35^\circ$, and 50°, respectively, in the incident plane $\varphi = 0^\circ$, corresponding to three different combinations of h_{gap} and h_{gap2}. (d) The total radiation patterns in one unit cell when different GBAs appeared for two polarization waves as marked in Fig. 5(c). The red line denotes p polarization and the blue line denotes s polarization.

As shown in Fig. 6(d), the experimental and simulated results of reflectance as a function of incident angle for the two incident planes ($\varphi = 0^\circ, 45^\circ$) at frequency $f = 28.025$ GHz which the dual-polarized wave realized GBE simultaneously are compared. Dual-polarized GBAs are both around 65° which is almost equal to the p-polarized BA which is about 64.5° for $\varepsilon_{r2} = 4.4$ in theory. Obviously, for this arrangement, the meta-surfaces can almost have identical properties in all incident planes. As shown in Fig. 6(e), the adjustments of $h_{\text{gap}} = 1.2$ mm, 1.4 mm, and 3 mm can dynamically modulate the s-polarized GBAs of 25°, 45°, and 80°, respectively, which indicate the great modulated ability of h_{gap}. As shown in Fig. 6(f), to achieve modulations of s- and p-polarized GBAs simultaneously, the thickness of PMI foam slabs above and below the sample ① were altered to adjust h_{gap} and h_{gap2}, respectively. Corresponding to the three sets of parameters shown in Fig. 6(e), the GBAs of s and p polarization can be modulated to equal to 20°, 35°, and 50° at the frequencies $f = 27.31$, 27.1, and 26.7 GHz, respectively. Once again, all of these results can prove the effectiveness of arbitrary modulated abilities of the different polarized GBEs by adjustments of h_{gap} and h_{gap2}, which validated our design principle based on the GKE.

V. CONCLUSION

In summary, based on the GKE, a simple and general design principle which includes infinite possibilities has been proposed to realize a dual-polarized GBE on the arbitrary dielectric interface for any incident angles and polarizations. This principle can not only describe the realization of methods of single p-polarized or single s-polarized GBEs, but also give many potential combinations of two kinds of situations to realize a dual-polarized GBE, even for higher-order multipolar components. Apparently, our models also include all realizing methods of previous works. The core of our principle is that the artificial

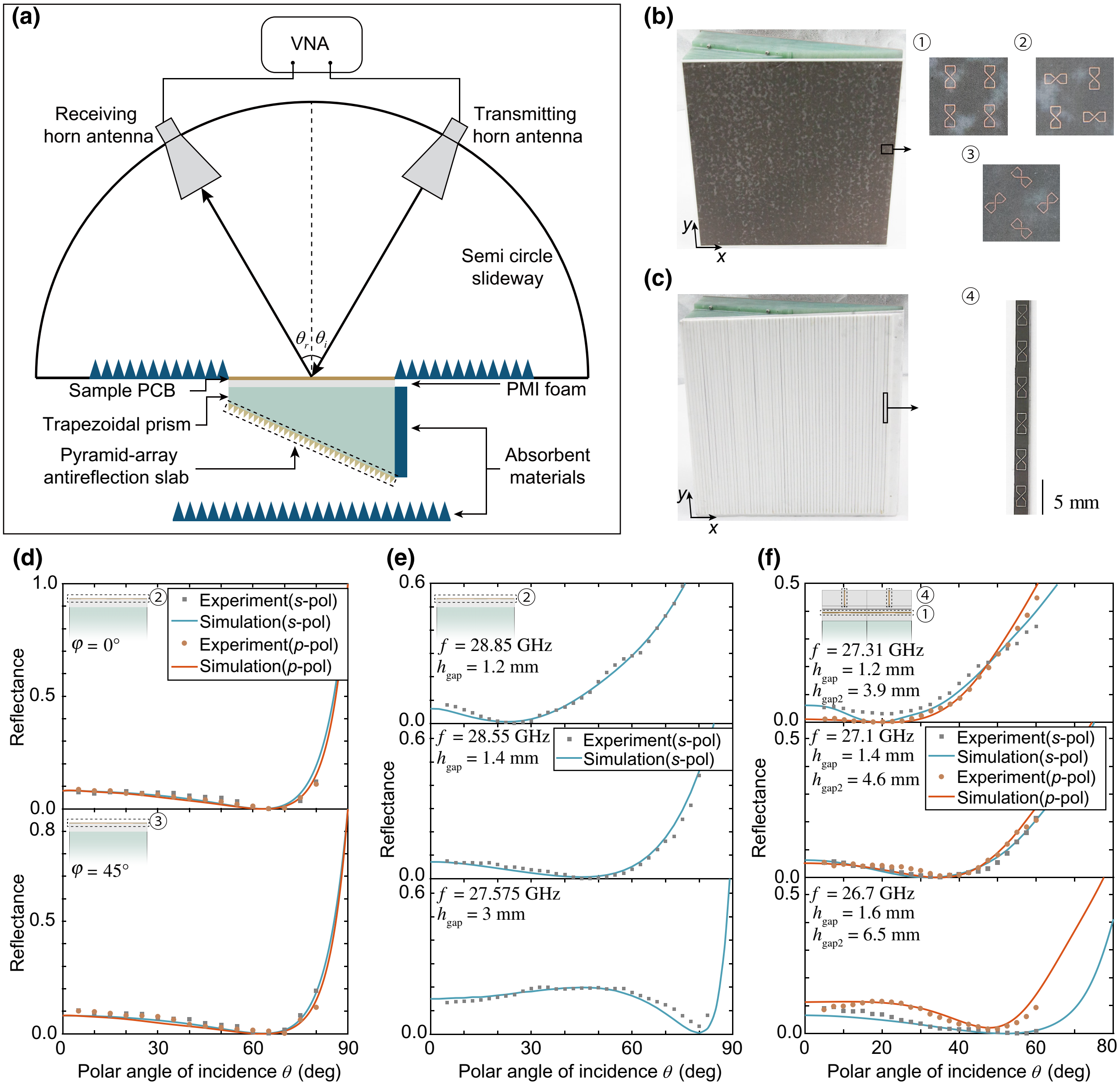

FIG. 6. The experimental instruments and results. (a) Schematic of the experimental instruments. (b),(c) Photos of the trapezoidal prism (Epoxy FRP, $\varepsilon_{r2} = 4.4$, $\tan\delta = 0.001$) to which samples and PMI foam slabs are fixed, and detailed photos of the PCB samples. In (b), the S ring planar array (marked with ①②③) which were printed on the back of PCB slab (Rogers RT / duroid 5880, $\varepsilon_{sub} = 2.2$, $h = 0.127$ mm, $\tan\delta = 0.0009$). (c) The dual-layer structure composed of ① and ④. (d) Fixing $h_{\text{gap}} = 1.8$ mm, results of experiment and simulation for s- and p-polarized incident waves in incident planes $\varphi = 0^\circ, 45^\circ$ correspond to planar samples ② and ③ at $f = 28.025$ GHz. (e) For planar sample ②, results of experiment and simulation for s-polarized incident waves in incident plane $\varphi = 0^\circ$ for $h_{\text{gap}} = 1.2$ mm, 1.4 mm, and 3 mm. (f) When placing the samples ① and ④, results of experiment and simulation for s- and p-polarized incident waves in incident plane $\varphi = 0^\circ$ through reasonable free controls of h_{gap} and h_{gap2}.

structures we add have independent and tunable responses for different polarizations. A metallic meta-surface has been designed. Using these meta-surfaces, we selected two combinations to validate our design principle, that is, we can only modulate s-polarized GBEs by meta-surface and utilize the self-exited p-polarized CBE, or we can separately modulate GBE of the dual-polarized wave by meta-surfaces with different electromagnetic wave polarized responses. The most important characteristic is that both of the solutions can achieve the GBE for the same incident angle and polarization at the same frequency. One parameter to modulate the GBE is changing the suspension

TABLE II. The geometric parameters of samples ①②③ shown in Fig. 6.

Parameters	d_{x1}	d_{x2}	d_y	p	w
Value/mm	0.6	0.7	1.15	4.7	0.08

height of meta-surfaces above the interface rather than the adjustments of many geometric parameters of structures. Using a microwave tested system, the experimental results correspond to simulated results of the fabricated sample, which indicates the validity and universality of this design theory. We believe that this work will open doors for easy-to-integrate and adjustable GBE devices which are not restricted to incident angles and polarizations.

ACKNOWLEDGMENTS

This work was supported by the China National Key Basic Research Program (2016YFA0301103, 2016YFA 0302000, and 2018YFA0306201) and the National Science Foundation of China (11774063, 11727811, 91750102, and 91963212). L.S. was further supported by the Science and Technology Commission of Shanghai Municipality (19XD1434600, 2019SHZDZX01, and 19DZ2253000).

APPENDIX A: THE QUANTITATIVE EQUIVALENT MODELS OF REFLECTION AND REFRACTION OF AN INCIDENT ELECTROMAGNETIC WAVE ON THE DIELECTRIC INTERFACE

Figure 7 shows a schematic diagram of equivalent models about refraction and reflection of an incident wave in this system. It is noted that the equivalent processes can be divided into two steps. First, the behaviors of refraction and reflection can be equivalent to directional radiation of an infinite ideal electric current sheet on the interface [43,51]. Second, connecting the properties of the electric current sheet to a discrete infinite phased array, the specific value of each dipole moment can be obtained [42]. The following text explains the processes separately.

1. s-polarized incident wave

As shown in Fig. 7(a), for the s-polarized wave, it is apparent that reflection and refraction plane waves can be equivalent to a radiated plane wave through infinite ideal electric current sheet along the y axis direction [43,51]. For this kind of infinite electric current sheet, electric and magnetic fields of the radiated plane wave in the upper space ($z > 0$) and lower space ($z < 0$) are

$$z > 0,$$

$$\boldsymbol{E_1} = A\eta_d\hat{y}e^{-ik_d(z\cos\theta_i + x\sin\theta_i)} \qquad \text{(A1)}$$

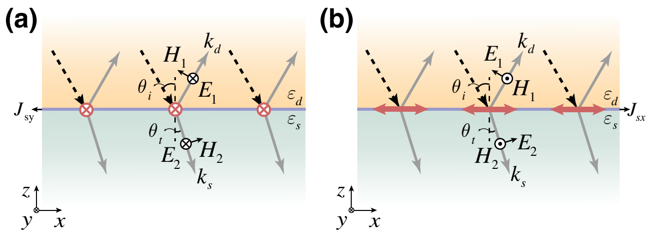

FIG. 7. The main situation discussed in this work is that the upper half-space and lower half-space are full of the different dielectrics whose permittivities are ε_d and ε_s, respectively. (a),(b) Refraction and reflection can be equivalent to directional radiation of a infinite ideal electric current sheet on the interface between upper and lower half-spaces (solid gray arrows). The surface electric current density on the two different infinite electric current sheets are denoted by $\boldsymbol{J_{sx}} = J_{0x}\hat{x}$ and $\boldsymbol{J_{sy}} = J_{0y}\hat{y}$, respectively. Here k_d and k_s denote wave vectors that the electromagnetic wave transmitted in the different dielectric. The equivalent processes of the s-polarized wave are shown in (a), resulting in surface electric current density along the y axis direction. The equivalent processes of the p-polarized wave are shown in (b), resulting in surface electric current density along the x axis direction.

$$\boldsymbol{H_1} = A(-\hat{x}\cos\theta_i + \hat{z}\sin\theta_i)e^{-ik_d(z\cos\theta_i + x\sin\theta_i)}, \qquad \text{(A2)}$$

$$z < 0,$$

$$\boldsymbol{E_2} = B\eta_s\hat{y}e^{ik_s(z\cos\theta_t - x\sin\theta_t)} \qquad \text{(A3)}$$

$$\boldsymbol{H_2} = B(\hat{x}\cos\theta_t + \hat{z}\sin\theta_t)e^{ik_s(z\cos\theta_t - x\sin\theta_t)}, \qquad \text{(A4)}$$

where A and B are amplitude constants, $\eta_d = \sqrt{\mu_d\varepsilon_d}$ and $\eta_s = \sqrt{\mu_s\varepsilon_s}$ are wave impedance for the two different dielectrics, θ_i and θ_t are the incident angle and refracted angle, respectively, which satisfy $\sqrt{\mu_d\varepsilon_d}\sin\theta_i = \sqrt{\mu_s\varepsilon_s}\sin\theta_t$ based on Snell's law.

And then forcing boundary conditions on the $z = 0$ interface for Eqs. (A1)–(A4):

$$\hat{z} \times (\boldsymbol{E_1} - \boldsymbol{E_2})|_{z=0} = -A\eta_d\hat{x}e^{-ik_dx\sin\theta_i} + B\eta_s\hat{x}e^{-ik_sx\sin\theta_t} = 0, \qquad \text{(A5)}$$

$$\hat{z} \times (\boldsymbol{H_1} - \boldsymbol{H_2})|_{z=0} = -A\cos\theta_i\hat{y}e^{-ik_dx\sin\theta_i} - B\cos\theta_t\hat{y}e^{-ik_sx\sin\theta_t} = J_{0y}\hat{y}. \qquad \text{(A6)}$$

Solving Eqs. (A5) and (A6), the expressions of A and B are

$$A = -\frac{\eta_s J_{0y}}{\eta_s\cos\theta_i + \eta_d\cos\theta_t}e^{ik_dx\sin\theta_i}, \qquad \text{(A7)}$$

$$B = -\frac{\eta_d J_{0y}}{\eta_s\cos\theta_i + \eta_d\cos\theta_t}e^{ik_dx\sin\theta_i}. \qquad \text{(A8)}$$

It is assumed that the complex Poynting vector $\boldsymbol{S}_{\text{in}}$ of the incident wave is known. In fact, the complex Poynting vector $\boldsymbol{S}_1$ and $\boldsymbol{S}_2$ of the reflection and refraction waves can be obtained by the Fresnel principle [51]. As the only goal is canceling the reflection wave from the interface, we can move focus to the $z > 0$ space. Using the definition formula of a complex Poynting vector, the relation of $\boldsymbol{S}_1$ and J_{0y} is

$$\boldsymbol{S}_1 = \boldsymbol{E}_1 \times \boldsymbol{H}_1{}^* = |A|^2 \eta_d (\hat{x} \sin\theta_i + \hat{z} \cos\theta_i). \tag{A9}$$

As there are only x and z components in $\boldsymbol{S}_1$, the electric current density J_{0y} may be the only contained z component S_{1z}:

$$\boldsymbol{J}_{sy} = \sqrt{\frac{S_{1z}(\cos\theta_i + \frac{\eta_d}{\eta_s}\cos\theta_t)^2}{\eta_d \cos\theta_i}}\hat{y}. \tag{A10}$$

Then, the surface electric current sheet will be equivalent to a discrete infinite point dipole phased array [42] by

$$p_y = s \cdot J_{sy}, \tag{A11}$$

where s denotes the area of a unit cell and p_y is the value of an ideal point dipole moment in a unit cell. Equation (A11) shows a simple relation of the y axis direction infinite dipole phased array and electric current sheet.

2. p-polarized incident wave

For equivalent model of p-polarized incident wave, the quantitative expression based on surface electric current sheet is difference from the traditional qualitative interpretation. As shown in Fig. 7(b), the direction of magnetic field of reflection and refraction wave is always perpendicular to x–z plane, causing one situation is that the radiation source can be equivalent to magnetic current sheet on the interface along y-axis direction. Conveniently, based on duality principle, the radiation field of this magnetic current sheet is identical with electric current sheet along x axis direction [51]. Similar to the situation in Appendix 1, the relation of S_{1z} and J_{0x} is

$$S_{1z} = \frac{|J_{0x}|^2 \eta_d \cos\theta_i}{(1 + \frac{\eta_d \cos\theta_i}{\eta_s \cos\theta_t})^2}. \tag{A12}$$

Thus, the electric current density J_{0x} can be expressed as

$$\boldsymbol{J}_{sx} = \sqrt{\frac{S_{1z}(1 + \frac{\eta_d \cos\theta_i}{\eta_s \cos\theta_t})^2}{\eta_d \cos\theta_i}}\hat{x}. \tag{A13}$$

Similarly, the relation of the infinite dipole phased array and electric current sheet along the x axis direction is

$$p_x = s \cdot J_{sx}. \tag{A14}$$

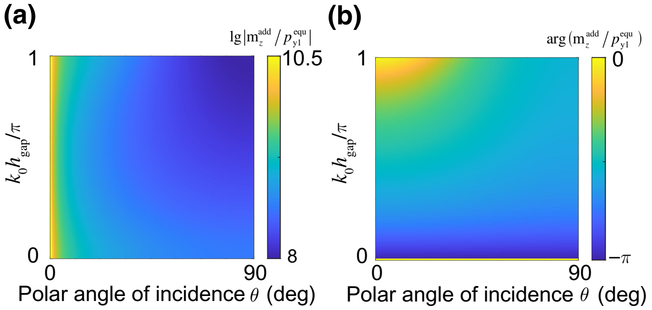

FIG. 8. For the case shown in Fig. 1(c), according to Eq. (3) from the condition of the GKE, we can obtain relations of the magnitude and phase of $m_z^{\rm add}/p_{y1}^{\rm equ}$ with respect to the incident angle and suspension height. (a) Logarithm of $|m_z^{\rm add}/p_{y1}^{\rm equ}|$ as a function of the suspension height (normalized by k_0/π) and incident angle. (b) Phase of $m_z^{\rm add}/p_{y1}^{\rm equ}$ as a function of the suspension height (normalized by k_0/π) and incident angle.

APPENDIX B: THE EFFECTS OF SUSPENSION HEIGHT

As shown in Fig. 8, $p_{y1}^{\rm equ}$ is almost unchangeable when the angle and frequency of incidence are fixed, resulting in the variation of magnitude of $m_z^{\rm add}$ required to achieve the GBE is very flat compared with $h_{\rm gap}$. However, the variation of the phase of $m_z^{\rm add}$ is fluctuating compared with $h_{\rm gap}$. There are two important facts: first, there are infinite solutions which can achieve the GBE for any incident angle apparently, which proves that the theoretical solutions of the GKE are ubiquitous in this case; second, a predictable fact is that the adjustments of $h_{\rm gap}$ must change the equivalent multipoles excited by the incident wave because of medium 2 which is full of lower half-space. As shown in Fig. 8, the GKE conditions can be satisfied by effective adjustments of this degree of freedom. To go a step further, the GBE of a system may be adjusted extremely flexibly without changing other parameters such as the shape of structures and so on. It will have extensive applications in many scenarios.

APPENDIX C: MULTIPOLE SUPERPOSITION EXPRESSIONS OF OTHER SITUATIONS

1. s-polarized incident wave

In Sec. II, only one situation which is shown in Fig. 1(c) has been specifically analyzed by the GKE. In order to illustrate the versatility and universality of this method as far as possible, the expressions of dipole components in other situations shown in Fig. 1 will be stated in this appendix [44,50,52–57].

As shown in Figs. 1(b) and 1(c), s-polarized wave impinges onto the interface from air. Similar to the process in Sec. II, the reflection and refraction waves can be equivalent to the radiation of an infinite electric dipole phased array along the y axis direction as shown in Appendix 1.

The spherical coordinate form of the far electric field of each equivalent point electric dipole along the y axis direction can be expressed by

$$E^{\mathrm{equ}}_{p1\varphi} = \frac{k_0^2 e^{ik_0 r}}{4\pi\varepsilon_0 r}(1+r_s)p^{\mathrm{equ}}_{y_1}. \tag{C1}$$

The $E^{\mathrm{equ}}_{p1\theta}$ of the electric dipole along the y axis direction is zero in this incident plane ($\varphi = 0^\circ$). For the situation as shown in Fig. 1(c), it is assumed that the direction of magnetic dipole is along the z axis direction. Apparently, it is different from the situation of multipoles in air, as the influence of the dielectric must be included. We assume that the location of the electric dipole on the interface is the origin of coordinates. Using a dyadic Green's function, by approximation of the far-field, the spherical coordinate forms of the electric field expression of each dipole component in the top half-space are

$$E^{\mathrm{add}}_{m\varphi} = \sqrt{\frac{\mu_0}{\varepsilon_0}}\,\frac{k_0^2 e^{ik_0(r-\boldsymbol{n}\cdot\boldsymbol{r_0})}}{4\pi r}\left(1+r_s e^{ik_0 2h_{\mathrm{gap}}\cos\theta}\right)m^{\mathrm{add}}_z \sin\theta, \tag{C2}$$

where ε_0 and μ_0 are vacuum permittivity and vacuum permeability, respectively, $k_0 = 2\pi/\lambda_0$ is the wave vector in vacuum, λ_0 is the wavelength of the incident electromagnetic wave in vacuum, r is distance from the origin to the view point, $\boldsymbol{n} = \boldsymbol{r}/r$ is the unit vector along the $\boldsymbol{r}$ direction, $\boldsymbol{r_0}$ is the position vector of the magnetic dipole in one unit cell, and $r_s = (\cos\theta - \sqrt{\varepsilon_r/\varepsilon_0 - \sin^2\theta})/(\cos\theta + \sqrt{\varepsilon_r/\varepsilon_0 - \sin^2\theta})$ is the reflection coefficient of the s-polarized incident wave on the interface.

In addition, for the situation shown in Fig. 1(b), the expression of the far electric field of an electric dipole along the y axis direction suspended above the interface at height h_{gap} is

$$E^{\mathrm{add}}_{p2\varphi} = \frac{k_0^2 e^{ik_0(r-\boldsymbol{n}\cdot\boldsymbol{r_0})}}{4\pi\varepsilon_0 r}\left(1+r_s e^{ik_0 2h_{\mathrm{gap}}\cos\theta}\right)p^{\mathrm{add}}_{y_2}. \tag{C3}$$

2. p-polarized incident wave

As shown in Figs. 1(e) and 1(f), they are different from the cases expressed in Appendix 1. With the perspective of Appendix 2, the reflection and refraction waves can be equivalent to the radiation of an infinite electric dipole phased array along the x axis direction. Thus, the spherical coordinate form of the electric far-field of each equivalent point electric dipole along the x axis direction can be expressed as

$$E^{\mathrm{equ}}_{p1\theta} = \frac{k_0^2 e^{ik_0 r}}{4\pi\varepsilon_0 r}(1-r_p)p^{\mathrm{add}}_{x_1}\cos\theta, \tag{C4}$$

where $r_p = (\varepsilon_r\cos\theta - \varepsilon_0\sqrt{\varepsilon_r/\varepsilon_0 - \sin^2\theta})/(\varepsilon_r\cos\theta + \varepsilon_0\sqrt{\varepsilon_r/\varepsilon_0 - \sin^2\theta})$ is the reflection coefficient of the p-polarized incident wave on the interface. The $E^{\mathrm{equ}}_{p1\varphi}$ of the electric dipole along the x axis direction is zero in this incident plane ($\varphi = 0^\circ$). For the situation as shown in Fig. 1(e), the electric far-field of each x axis direction electric dipole suspended above the interface can be expressed as

$$E^{\mathrm{add}}_{p2\theta} = \frac{k_0^2 e^{ik_0(r-\boldsymbol{n}\cdot\boldsymbol{r_0})}}{4\pi\varepsilon_0 r}\left(1-r_p e^{ik_0 2h_{\mathrm{gap}}\cos\theta}\right)p^{\mathrm{add}}_{x_2}\cos\theta. \tag{C5}$$

For the situation shown in Fig. 1(f), the electric far-field of each magnetic dipole along the y axis direction suspended above the interface is

$$E^{\mathrm{add}}_{m\theta} = \sqrt{\frac{\mu_0}{\varepsilon_0}}\,\frac{k_0^2 e^{ik_0(r-\boldsymbol{n}\cdot\boldsymbol{r_0})}}{4\pi r}\left(1+r_p e^{ik_0 2h_{\mathrm{gap}}\cos\theta}\right)m^{\mathrm{add}}_y. \tag{C6}$$

APPENDIX D: THE DESIGN PRINCIPLES OF TRAPEZOIDAL PRISM AND PYRAMID-ARRAY ANTIREFLECTION SLAB

The design principles and functions of PAS grating structures have been discussed in detail in many works [58–60]. According to the design theories from previous researchers, the gradually changed geometric parameters of structures can be reversely designed according to the gradient range of the refractive index. In particular, for small incident angle, the impedance matching property of this structure is good. Figure 9(a) is a schematic diagram of a PAS (WL F4BTM-1/2, tan$\delta = 0.0015$, period is $p = 4.7$ mm, height of pyramids is $h = 10$ mm). By the design of the PAS geometric parameters, from the reflectance spectrum at $f = 28$ GHz as shown in Fig. 9(b), it can be clearly seen that the reflectance is almost close to zero when the incident angle is less than 30°, after which the reflectivity will gradually increase. It can be seen from the above results that we can utilize the excellent antireflection performance of this structure to make a substrate system that is very close to only reflecting on the interface without any film interference phenomena for any incident angles.

As shown in Fig. 9(c), the electromagnetic wave will reflect and refract on plane B for any incident angle. To eliminate reflection as far as possible when the refracted wave impinges onto plane A, the PAS can be fixed on this plane. However, the results in Fig. 9(b) have shown that larger incident angle will weaken the antireflection effect of the structure. It is clearly that the adjustment of the included angle θ_p for planes A and B can determine the shape of this trapezoidal prism to minimize the incident angle on plane A. Owing to the wide range of incident angle which verification experiments required, the included angle was selected as $\theta_p = 70^\circ$. Then, as shown in Fig. 9(d), based on Snell's law and geometric relations, the relation of incident angle θ_1 on plane A and θ_{i1} on plane B can be obtained. Clearly, $\theta_1 < 20^\circ$ for different θ_i, and, further, $\theta_1 < 10^\circ$ for the range of incident angle

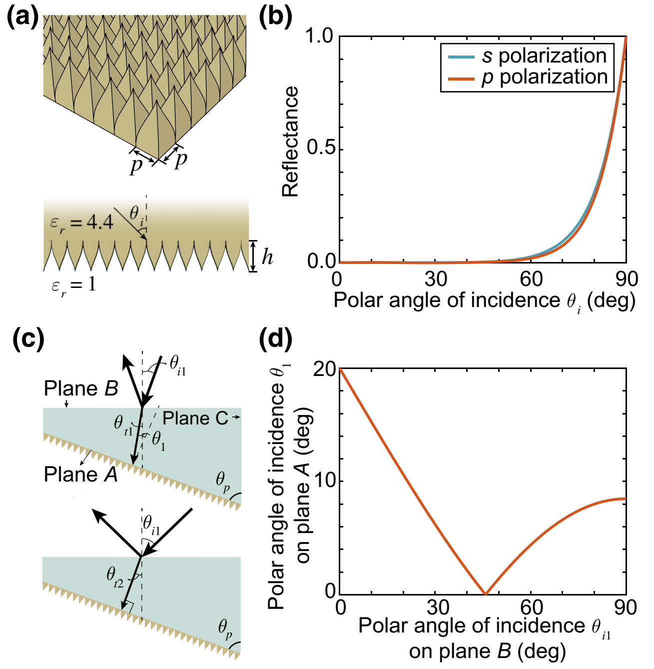

FIG. 9. The design process of a pyramid-array antireflection slab (PAS) fixed on a trapezoidal prism. (a) Schematic diagram of an ideal PAS and propagation of the electromagnetic wave on the interface (incident angle is θ_i). The period of the PAS unit cell is $p = 4.7$ mm, and the relative permittivity of the material is $\varepsilon_{r2} = 4.4$. (b) For the structure system as shown in Fig. 9(a), the reflectance as a function of incident angle when the electromagnetic wave impinges onto vacuum at angle θ_i. (c) Schematic diagram of the propagation process when an electromagnetic wave impinges onto a trapezoidal prism whose back fixed PAS. (d) The incident angle θ_1 on plane A as a function of incident angle θ_{i1} on plane B for $\theta_p = 70°$.

($\theta_i \in [20°, 80°]$) with which this article is concerned. It is worth noting that for the three-dimensional gradual structure with such small size, considering the difficulty of actual fabrication and actual properties, the PAS used in experiments was obtained from a 10-mm-thick PCB slab which was cut into a 64 × 71 pyramid array to realize almost the same transmission performance.

APPENDIX E: THE HIGH-ORDER DIFFRACTIONS AND ELIMINATED METHOD

For the structure of Fig. 4(a), the high-order diffractions will appear at incident angle $\theta = 62°$ at frequency $f = 28.85$ GHz because the size of the unit cell is $2p = 10$ mm. As shown in Fig. 10, when the s-polarized plane wave impinges, the diffracted efficiency of this structure can be obtained at an angle of incidence of $\theta = 62°$ for the two different incident planes ($\varphi = 0°, \varphi = 45°$). For the high-order transmitted diffractions, as shown in Figs. 10(a) and 10(b), in addition to the fundamental modes, there is only very low efficiency for the $[0, -2]$ order TE mode in incident plane ($\varphi = 0°$) and $[0, -2]$, $[-2, 0]$ order TE modes in incident plane ($\varphi = 45°$). It is worth noting that all other-order transmitted diffractions whose efficiencies are extremely close to zero are not shown in Figs. 10(a) and 10(b). Clearly, for other high-order reflected diffractions, as shown in Figs. 10(c) and 10(d), the efficiency of all other-order reflected diffractions are really close to zero for the two incident planes. Thus, in fact, there is hardly any energy being reflected at this incident angle. However, there is little energy being transmitted in other directions besides the normal refracted direction.

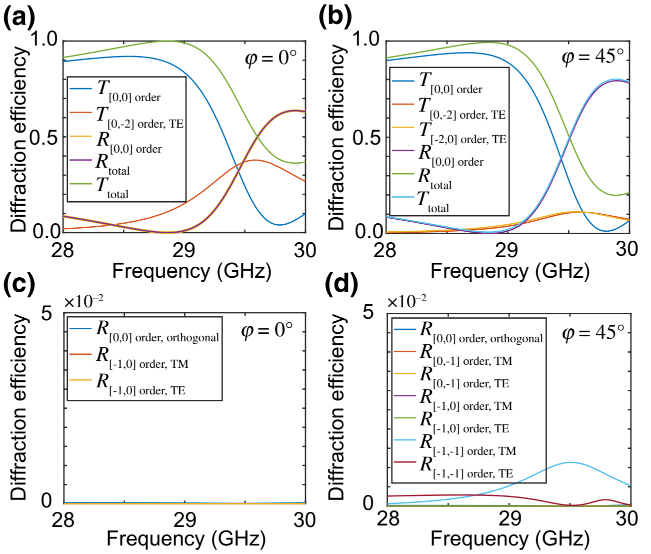

FIG. 10. The diffraction efficiency of the structure in Fig. 4(a) at angle of incidence of $\theta = 62°$ for the two typical incident planes $\varphi = 0°$ and $\varphi = 45°$. (a),(b) The diffraction efficiency of fundamental modes and nonzero higher-order modes for the incident planes $\varphi = 0°$ and $\varphi = 45°$, respectively. (c),(d) The diffraction efficiency of all other-order reflected modes for the incident planes $\varphi = 0°$ and $\varphi = 45°$, respectively.

As shown in Figs. 11(a) and 11(b), in order to eliminate the high-order diffractions and maintain the 90° rotational symmetry, we decreased the period to $p = 5$ mm and adjusted the size of the structure. As shown in Figs. 11(c) and 11(d), similar to Figs. 4(c) and 4(d) in the main text, the GBE was realized in all incident planes ($\varphi = 0°$–$90°$) at almost the same frequency ($f = 28.5$ GHz) when s-polarized plane wave impinges at an angle $\theta = 62°$. Responses are really very weak for the incidence of a p-polarized wave at the same incident angle, resulting in the situation that GBE can be realized at the whole frequency range. As shown in Figs. 11(e) and 11(f), for s-polarized GBE at $f = 28.5$ GHz, the reflectance of dual-polarized waves as functions of incident angle theta are almost identical for the two different incident planes. Anyway, we not only eliminate any high-order diffractions by decreasing the size of unit cell to $p = 5$ mm, but also

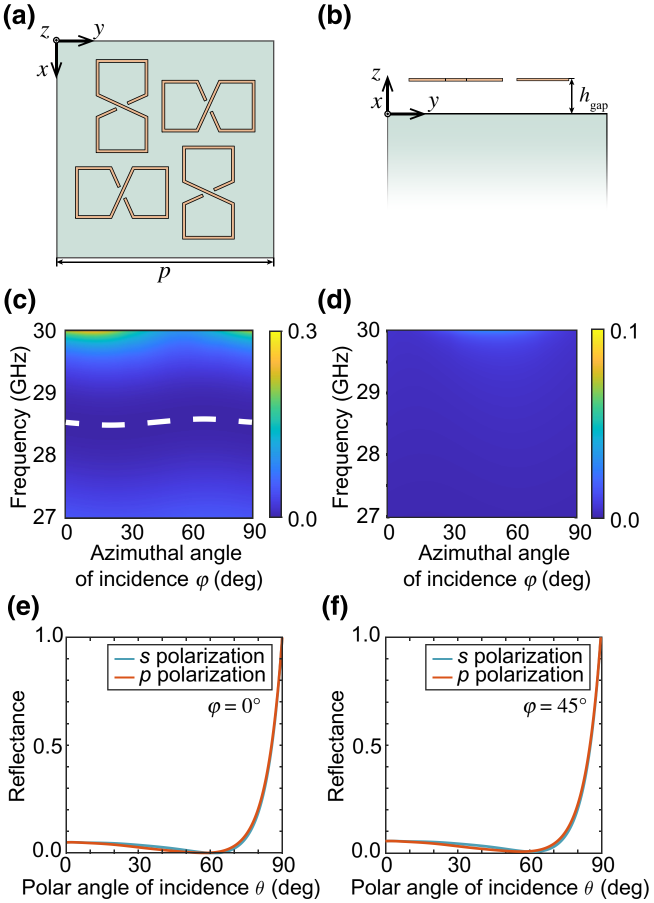

FIG. 11. Schematic and simulated results of modified 90° symmetrical S ring meta-surface with $p = 5$ mm. (a),(b) The modified S ring structures are arranged with 90° rotational symmetry periodically. (c),(d) The reflectance as a function of azimuthal angle of incidence and frequency when s- or p-polarized plane wave impinges at an angle $\theta = 62°$. The white dashed line indicates the GBA of s polarization from $\varphi = 0°$ to $\varphi = 90°$. (e),(f) At $f = 28.5$ GHz, the reflectance of two kinds of polarized waves as functions of incident angle θ when incident planes are $\varphi = 0°$ and $\varphi = 45°$, respectively.

almost maintain the same properties of the GBE through a similar structure with different parameters.

APPENDIX F: THE DETAILS OF NUMERICAL CALCULATION

The reflection and volume current density simulations are conducted using finite element methods (COMSOL MULTIPHYSICS). The three-dimensional simulation domain consists of a unit cell with periodic boundary conditions applied in two directions (x and y axes). In the z axis direction, the excited port is used at the top of an air box to simulate the illumination of plane wave (s or p polarization) in different angles, and the received port is used at the bottom of a dielectric box to make sure that no energy can be reflected on this plane. A frequency domain study is used to sweep the incident frequency of the plane wave, and the incident angle or plane can be changed continuously through parametric sweep. When the GBE is realized at one incident angle θ_B, we need to extract the volume current density of the S ring in the unit cell to perform multipole expansion [12,61].

[1] D. Brewster, On the laws which regulate the polarisation of light by reflexion from transparent bodies, Philos. Trans. R. Soc. London **105**, 125 (1815).

[2] C. L. Giles and W. J. Wild, Brewster angles for magnetic media, Int. J. Infrared Millimeter Waves **6**, 187 (1985).

[3] V. G. Veselago, Electrodynamics of substances with simultaneously negative and, Usp. Fiz. Nauk **92**, 517 (1967).

[4] J. B. Pendry, A. J. Holden, D. J. Robbins, and W. Stewart, Magnetism from conductors and enhanced nonlinear phenomena, IEEE Trans. Microw. Theory Tech. **47**, 2075 (1999).

[5] D. R. Smith, W. J. Padilla, D. Vier, S. C. Nemat-Nasser, and S. Schultz, Composite Medium with Simultaneously Negative Permeability and Permittivity, Phys. Rev. Lett. **84**, 4184 (2000).

[6] J. B. Pendry, Negative Refraction Makes a Perfect Lens, Phys. Rev. Lett. **85**, 3966 (2000).

[7] R. Marques, J. Martel, F. Mesa, and F. Medina, Left-Handed-Media Simulation and Transmission of em Waves in Subwavelength Split-Ring-Resonator-Loaded Metallic Waveguides, Phys. Rev. Lett. **89**, 183901 (2002).

[8] N. I. Zheludev and Y. S. Kivshar, From metamaterials to metadevices, Nat. Mater. **11**, 917 (2012).

[9] A. Poddubny, I. Iorsh, P. Belov, and Y. Kivshar, Hyperbolic metamaterials, Nat. Photonics **7**, 948 (2013).

[10] H. Wu, D. Kong, Z. Ruan, P.-C. Hsu, S. Wang, Z. Yu, T. J. Carney, L. Hu, S. Fan, and Y. Cui, A transparent electrode based on a metal nanotrough network, Nat. Nanotechnol. **8**, 421 (2013).

[11] S. B. Glybovski, S. A. Tretyakov, P. A. Belov, Y. S. Kivshar, and C. R. Simovski, Metasurfaces: From microwaves to visible, Phys. Rep. **634**, 1 (2016).

[12] W. Liu, Generalized Magnetic Mirrors, Phys. Rev. Lett. **119**, 123902 (2017).

[13] C. Fu, Z. M. Zhang, and P. N. First, Brewster angle with a negative-index material, Appl. Opt. **44**, 3716 (2005).

[14] T. Tanaka, A. Ishikawa, and S. Kawata, Unattenuated light transmission through the interface between two materials with different indices of refraction using magnetic metamaterials, Phys. Rev. B **73**, 125423 (2006).

[15] Y. Tamayama, T. Nakanishi, K. Sugiyama, and M. Kitano, Observation of Brewster's effect for transverse-electric electromagnetic waves in metamaterials: Experiment and theory, Phys. Rev. B **73**, 193104 (2006).

[16] R. Watanabe, M. Iwanaga, and T. Ishihara, s-polarization Brewster's angle of stratified metal–dielectric metamaterial in optical regime (2008).

[17] X. Lin, Y. Shen, I. Kaminer, H. Chen, and M. Soljačić, Transverse-electric Brewster effect enabled by nonmagnetic two-dimensional materials, Phys. Rev. A **94**, 023836 (2016).

[18] W. Shu, Z. Ren, H. Luo, and F. Li, Brewster angle for anisotropic materials from the extinction theorem, Appl. Phys. A **87**, 297 (2007).

[19] Y. Tamayama, Brewster effect in metafilms composed of bi-anisotropic split-ring resonators, Opt. Lett. **40**, 1382 (2015).

[20] H. Mahlein, Generalized Brewster-angle conditions for quarter-wave multilayers at non-normal incidence, JOSA **64**, 647 (1974).

[21] J. Heading, Generalized investigations into the Brewster angle, Optica Acta: Int. J. Opt. **33**, 755 (1986).

[22] R. Paniagua-Domínguez, Y. F. Yu, A. E. Miroshnichenko, L. A. Krivitsky, Y. H. Fu, V. Valuckas, L. Gonzaga, Y. T. Toh, A. Y. S. Kay, and B. Luk'yanchuk *et al.*, Generalized Brewster effect in dielectric metasurfaces, Nat. Commun. **7**, 1 (2016).

[23] K. V. Sreekanth, M. ElKabbash, R. Medwal, J. Zhang, T. Letsou, G. Strangi, M. Hinczewski, R. S. Rawat, C. Guo, and R. Singh, Generalized Brewster angle effect in thin-film optical absorbers and its application for graphene hydrogen sensing, ACS Photonics **6**, 1610 (2019).

[24] S. Yin and J. Qi, Metagrating-enabled Brewster's angle for arbitrary polarized electromagnetic waves and its manipulation, Opt. Express **27**, 18113 (2019).

[25] Z. Wu, M. Zhou, E. Khoram, B. Liu, and Z. Yu, Neuromorphic metasurface, Photonics Res. **8**, 46 (2020).

[26] Z. Ruan and M. Qiu, Enhanced Transmission through Periodic Arrays of Subwavelength Holes: The Role of Localized Waveguide Resonances, Phys. Rev. Lett. **96**, 233901 (2006).

[27] C. R. Simovski, P. A. Belov, A. V. Atrashchenko, and Y. S. Kivshar, Wire metamaterials: Physics and applications, Adv. Mater. **24**, 4229 (2012).

[28] Y. Lou, H. Pan, T. Zhu, and Z. Ruan, Spatial coupled-mode theory for surface plasmon polariton excitation at metallic gratings, JOSA B **33**, 819 (2016).

[29] M. Zhou, J. Liu, M. A. Kats, and Z. Yu, Optical metasurface based on the resonant scattering in electronic transitions, ACS Photonics **4**, 1279 (2017).

[30] A. H. Dorrah, M. Chen, and G. V. Eleftheriades, Bianisotropic Huygens' metasurface for wideband impedance matching between two dielectric media, IEEE Trans. Antennas Propag. **66**, 4729 (2018).

[31] A. S. Kupriianov, Y. Xu, A. Sayanskiy, V. Dmitriev, Y. S. Kivshar, and V. R. Tuz, Metasurface Engineering through Bound States in the Continuum, Phys. Rev. Appl. **12**, 014024 (2019).

[32] T. Feng, A. A. Potapov, Z. Liang, and Y. Xu, Huygens Metasurfaces Based on Congener Dipole Excitations, Phys. Rev. Appl. **13**, 021002 (2020).

[33] G. Lavigne and C. Caloz, in *2018 IEEE International Symposium on Antennas and Propagation & USNC/URSI National Radio Science Meeting* (IEEE, Boston, Massachusetts, USA, 2018), p. 771.

[34] S. Chatterjee, E. Shkondin, O. Takayama, A. V. Lavrinenko, M. Hinczewski, and G. Strangi, in *Nanophotonics VIII* (International Society for Optics and Photonics, 2020), Vol. 11345, p. 1134524.

[35] C. Wang, Z. Zhu, W. Cui, Y. Yang, L. Ran, and D. Ye, All-angle Brewster effect observed on a terahertz metasurface, Appl. Phys. Lett. **114**, 191902 (2019).

[36] G. Lavigne and C. Caloz, Generalized Brewster effect using bianisotropic metasurfaces, Opt. Express **29**, 11361 (2021).

[37] Z. Chen, X. Chen, L. Tao, K. Chen, M. Long, X. Liu, K. Yan, R. I. Stantchev, E. Pickwell-MacPherson, and J.-B. Xu, Graphene controlled Brewster angle device for ultra broadband terahertz modulation, Nat. Commun. **9**, 1 (2018).

[38] D. Hoenig and D. Moebius, Direct visualization of monolayers at the air-water interface by Brewster angle microscopy, J. Phys. Chem. **95**, 4590 (1991).

[39] V. Kravets, F. Schedin, R. Jalil, L. Britnell, R. Gorbachev, D. Ansell, B. Thackray, K. Novoselov, A. Geim, and A. V. Kabashin *et al.*, Singular phase nano-optics in plasmonic metamaterials for label-free single-molecule detection, Nat. Mater. **12**, 304 (2013).

[40] M. Kerker, D.-S. Wang, and C. Giles, Electromagnetic scattering by magnetic spheres, JOSA **73**, 765 (1983).

[41] W. Liu and Y. S. Kivshar, Generalized Kerker effects in nanophotonics and meta-optics, Opt. Express **26**, 13085 (2018).

[42] H. Wheeler, Simple relations derived fom a phased-array antenna made of an infinite current sheet, IEEE Trans. Antennas Propag. **13**, 506 (1965).

[43] D. M. Pozar, *Microwave Engineering* (John wiley & sons, Hoboken, NJ, USA, 2011).

[44] L. Novotny and B. Hecht, *Principles of Nano-Optics* (Cambridge university press, Cambridge, England, 2012).

[45] A. Bhattacharyya, in *BFNs and active array systems* (Wiley-Interscience, Hoboken, NJ, USA, 2006).

[46] W. L. Stutzman and G. A. Thiele, *Antenna Theory and Design* (John Wiley & Sons, Hoboken, NJ, USA, 2012).

[47] S. Mühlig, C. Menzel, C. Rockstuhl, and F. Lederer, Multipole analysis of meta-atoms, Metamaterials **5**, 64 (2011).

[48] P. Grahn, A. Shevchenko, and M. Kaivola, Electromagnetic multipole theory for optical nanomaterials, New J. Phys. **14**, 093033 (2012).

[49] J. D. Jackson, Classical electrodynamics (1999).

[50] A. E. Miroshnichenko, A. B. Evlyukhin, Y. S. Kivshar, and B. N. Chichkov, Substrate-induced resonant magnetoelectric effects for dielectric nanoparticles, ACS Photonics **2**, 1423 (2015).

[51] K. J. Au, *Electromagnetic Wave Theory* (Wiley, Hoboken, NJ, USA, 1986).

[52] W. Liu and Y. S. Kivshar, Multipolar interference effects in nanophotonics, Philos. Trans. R. Soc. A: Math. Phys. Eng. Sci. **375**, 20160317 (2017).

[53] A. B. Evlyukhin, C. Reinhardt, A. Seidel, B. S. Luk'yanchuk, and B. N. Chichkov, Optical response features of Si-nanoparticle arrays, Phys. Rev. B **82**, 045404 (2010).

[54] A. B. Evlyukhin, C. Reinhardt, and B. N. Chichkov, Multipole light scattering by nonspherical nanoparticles in the discrete dipole approximation, Phys. Rev. B **84**, 235429 (2011).

[55] A. B. Evlyukhin, C. Reinhardt, E. Evlyukhin, and B. N. Chichkov, Multipole analysis of light scattering by arbitrary-shaped nanoparticles on a plane surface, JOSA B **30**, 2589 (2013).

[56] L. Novotny, Allowed and forbidden light in near-field optics. II. Interacting dipolar particles, JOSA A **14**, 105 (1997).

[57] W. Liu, A. E. Miroshnichenko, D. N. Neshev, and Y. S. Kivshar, Broadband unidirectional scattering by magneto-electric core–shell nanoparticles, ACS Nano **6**, 5489 (2012).

[58] R. W. Klopfenstein, A transmission line taper of improved design, Proc. IRE **44**, 31 (1956).

[59] W. H. Southwell, Gradient-index antireflection coatings, Opt. Lett. **8**, 584 (1983).

[60] W. H. Southwell, Pyramid-array surface-relief structures producing antireflection index matching on optical surfaces, JOSA A **8**, 549 (1991).

[61] Z. Che, Y. Zhang, W. Liu, M. Zhao, J. Wang, W. Zhang, F. Guan, X. Liu, W. Liu, and L. Shi *et al.*, Polarization Singularities of Photonic Quasicrystals in Momentum Space, Phys. Rev. Lett. **127**, 043901 (2021).